Solid-State Phase Transition of Agomelatine-Phosphoric Acid Molecular Complexes Along the Salt–Cocrystal Continuum: *Ab initio* Powder-XRD Structure Determination and DFT-D2 Analysis

Supporting information

Raja Sekhar Voguri[a,b], Santosh Ranga[b], Archan Dey[a]* and **Subhas Ghosal[b,c]***

[a]Advanced Characterization Technology Lab, Integrated Product Development (IPDO), Dr. Reddy's Laboratories, Hyderabad, Telangana, India.

[b]Department of Chemistry, Birla Institute of Technology & Science, Pilani - Hyderabad Campus, Telangana, India.

[c] Department of Chemistry, National Institute of Technology Durgapur, Durgapur 713209, WB, India

Correspondence email: subhas.ghosal@ch.nitdgp.ac.in & archan_dey@yahoo.co.in

Table of Contents

Table S1 3
Fig. S1 6
Fig. S2 7
Fig. S3 8
Fig. S4 9
Fig. S6 11
Fig. S7 12

Fig. S8 13
Fig. S9 14
Fig. S10 15
Fig. S11 16
Fig. S12 17
Fig. S13 18

Table S1: Crystal structure survey of Agomelatine M-APIs

Sl. No.	Coformer	Reported (SXRD/PXRD)	Calculated (ΔpKa)	Agomelatine		References No *(Refer Bibliography)*
				d_{C-O}/d_{C-N} #	Torsion angle τ3	
1	Hydroquinone Form – I *	Cocrystal SXRD	Cocrystal (-11.3)	0.95	95.3	31
				0.94	99.0	
				0.93	93.1	
				0.94	91.1	
2	Hydroquinone Form - II	Cocrystal PXRD	Cocrystal (-11.3)	0.97	86.6	
3	Pyruvic acid	Cocrystal SXRD	Cocrystal (-3.8)	0.94	84.4	
4	Urea	Cocrystal SXRD	Cocrystal (-1.6)	0.93	85.7	
5	Oxalic acid i-1	Cocrystal SXRD	Cocrystal (-2.7)	0.96	89.8	
6	Oxalic acid i-1			0.96	86.7	
7	Acetic acid Form - I	Cocrystal SXRD	Cocrystal (-6.2)	0.94	84.5	30
8	Acetic acid Form - II	Cocrystal SXRD	Cocrystal (-6.2)	0.85	84.3	31
9	Ethylene glycol	Cocrystal PXRD	Cocrystal (-16.6)	0.93	90.0	30
10	Glycolic acid	Cocrystal SXRD	Cocrystal (-5.3)	0.93	80.3	35
11	Isonicotinamide	Cocrystal SXRD	Cocrystal (-4.8)	0.92	88.7	
12	Methyl 4-hydroxybenzoate	Cocrystal SXRD	Cocrystal (-10)	0.92	88.9	
13	Sulfuric acid	Salt PXRD	Cocrystal/ Salt (1.4)	1.00	93.5	33
14	Methanesulfonic acid	Salt SXRD	Cocrystal (-0.3)	0.99	73.7	

15	Benzenesulfonic acid	Salt SXRD	Cocrystal (-2.2)	1.00	92.2	
16	Hydrogensulfate methanol solvate hemihydrate	Salt SXRD	Cocrystal/ Salt (1.4)	1.00	81.6	
					86.8	
17	mesylate monohydrate	Salt SXRD	Cocrystal/ Salt (-0.3)	Salt (0.98)	175.4	
18	HI (AgI)	Salt SXRD	Salt (8.4)	1.01	94.0	34
19	HI (AgI3)			0.97	81.4	
20	HI (AgI2)*			0.96	88.6	
				0.96	90.2	
				0.97	91.8	
				0.96	94.0	
21	Phosphoric acid	Salt SRXRD	Cocrystal (-3.7)	Not available	Not available	36
22	Resorcinol	Cocrystal Not reported	Cocrystal (-10.7)	Not available	Not available	32
23	AGL Form – I	API SXRD	NA	0.94	103.2	30
				0.93	91.3	
				0.94	86.8	
				0.93	101.1	
24	AGL Form – II		NA	0.93	83.4	31
				0.94	96.7	
25	AGL Form – III		NA	0.93	86.0	
Crystal Structures in this Study						
26	AGL-P RT-Form (Rietveld-refined)	Cocrystal PXRD	Cocrystal (-3.7)	0.90	96.8	NA
25	AGL-P RT-Form	Salt PXRD	Salt (-3.7)	0.99	93.7	NA
27	AGL-P HT-Form (Rietveld-refined)	Cocrystal PXRD	Cocrystal (-3.7)	0.90	79.7	NA

28	AGL-P HT-Form	Cocrystal PXRD	Cocrystal (-3.7)	0.96	83.9	NA
*Z' = 4, # 1. As per isolated molecule: C-O/C-N criteria for cocrystal C-O/C-N≥0.82 and for salt C-O/C-N≤1.14; 2. As per CCDC: median ratio of the cocrystal (neutral amide) is 0.90 and salt (O-protonated amide) is 0.99						

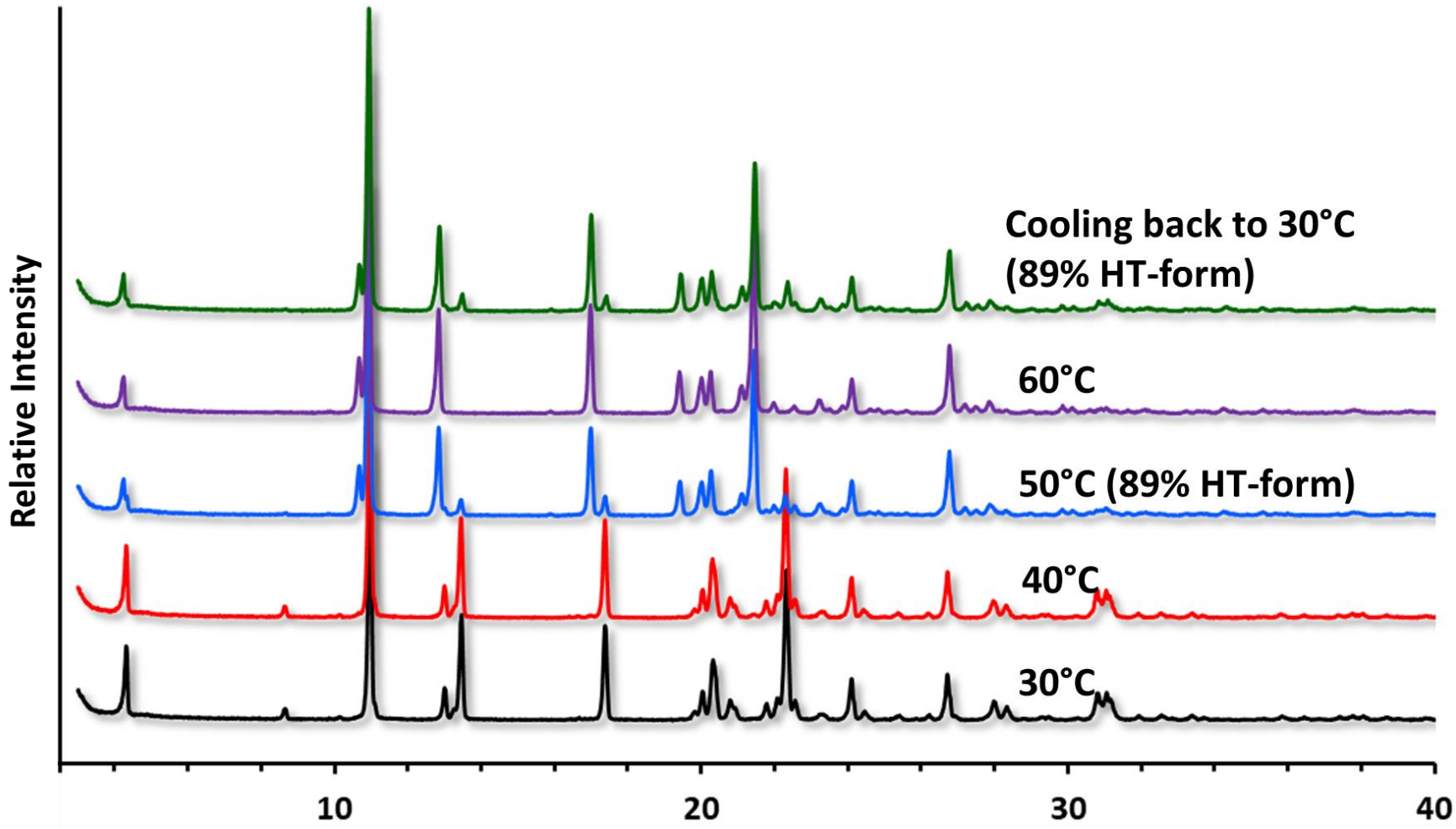

Fig. S1: Overlay of VT-PXRD powder-XRD data collected in the temperature range of 30°C to 60°C at each 10°C increment and at 30°C after cooling.

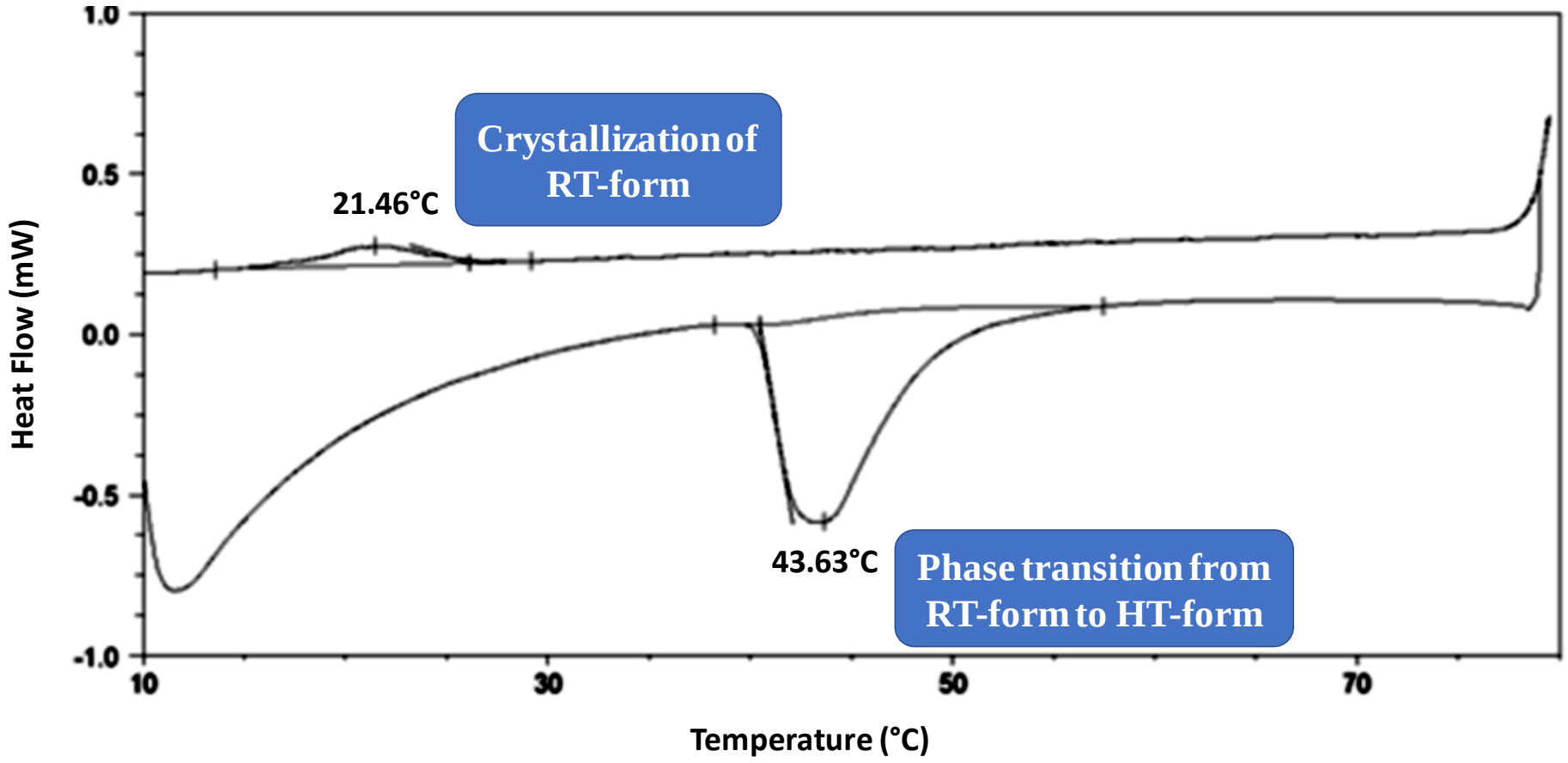

Fig. S2: DSC thermogram for the heat-cool cycle of AGL-P with phase transition and recrystallization events are indicated.

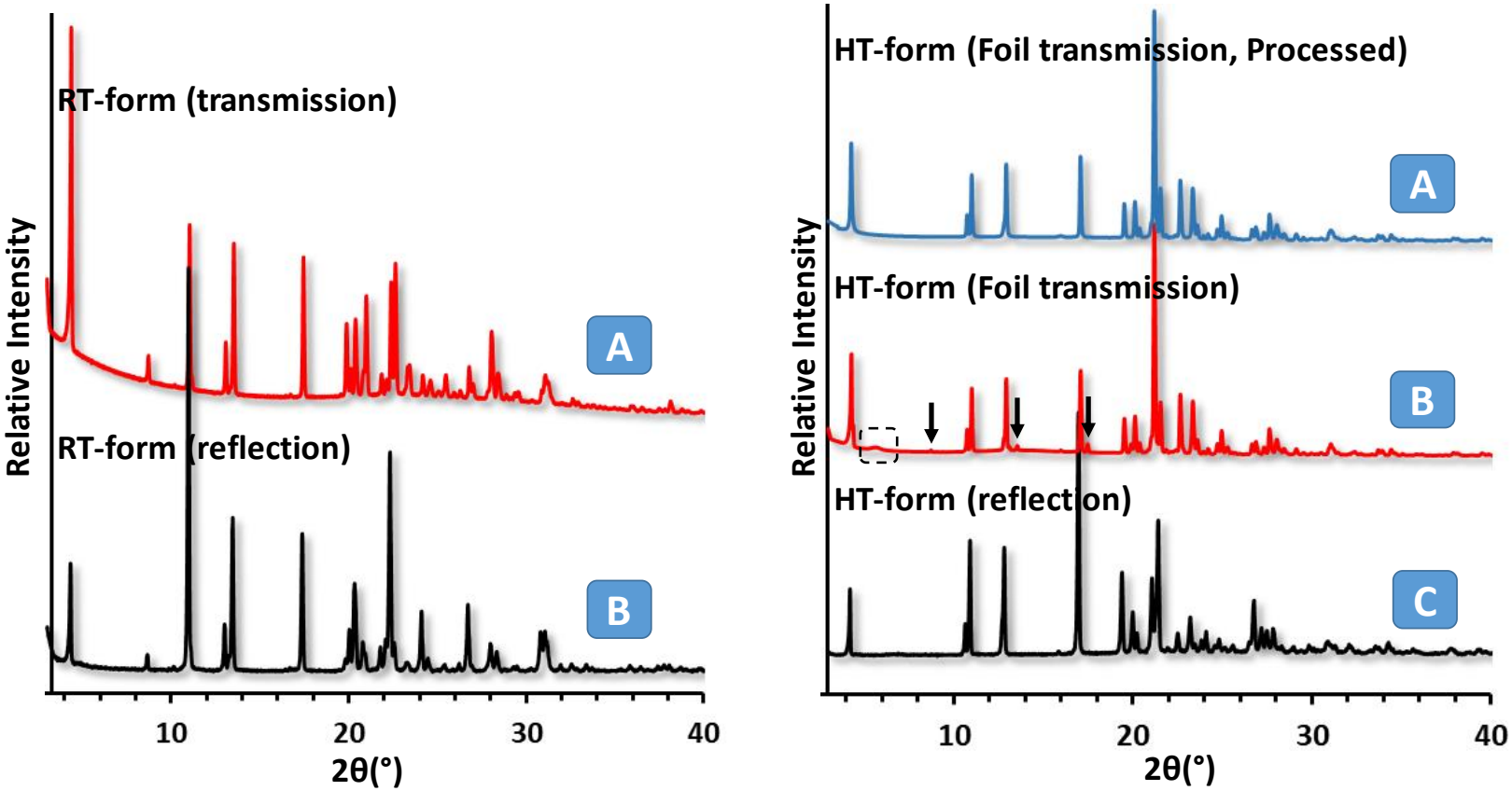

Fig. S3: Data collection strategy for SDPD by optimizing the factors: preferred orientation and rate of HT-form to RT-form conversion. Please note that peaks (marked with arrows) corresponding to the RT-form in HT-form data were trimmed. The broad beak peak indicated with the dotted box is corresponding to the background from foil used in foil transmission PXRD data collection.

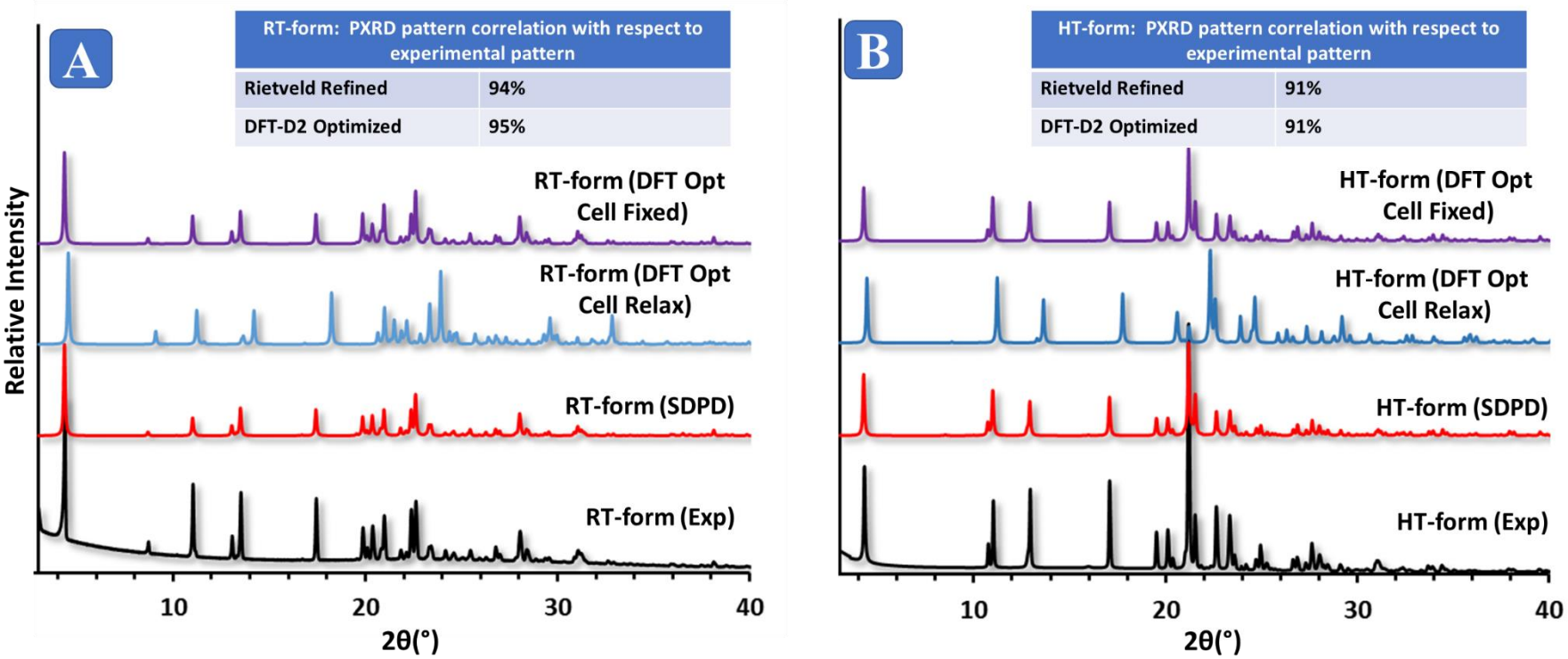

Fig. S4: Comparison of experimental powder XRD patterns with simulated PXRD patterns of crystal obtained using Rietveld-refinement, DFT optimization (with and without fixed cell) for (A) RT-form and (B) HT-form. DFT-D2 optimization with relaxed cell gave PXRD patterns with shifted peak positions as compared to the experimental PXRD pattern. Whereas Rietveld-refined and DFT-D2 optimized (with fixed cell) has given a better match with experimental PXRD patterns for both the forms. The % of correlation of simulated PXRD patterns of Rietveld-refined and DFT-D2 optimized with respect of experimental PXRD patterns is similar for HT-form, whereas 1% improvement observed for RT-form upon DFT optimization.

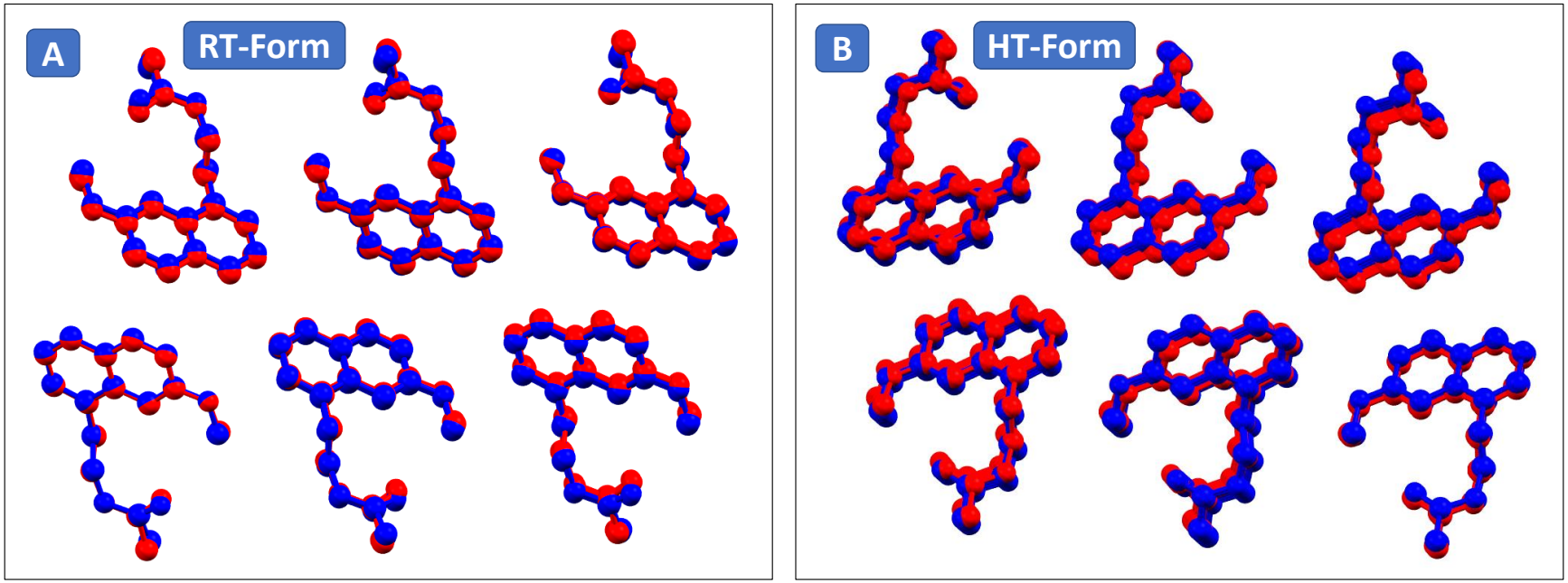

Fig. S5: Overlay of RT-form and HT-form crystal structures Rietveld-refined (red) and DFT-optimized (blue).

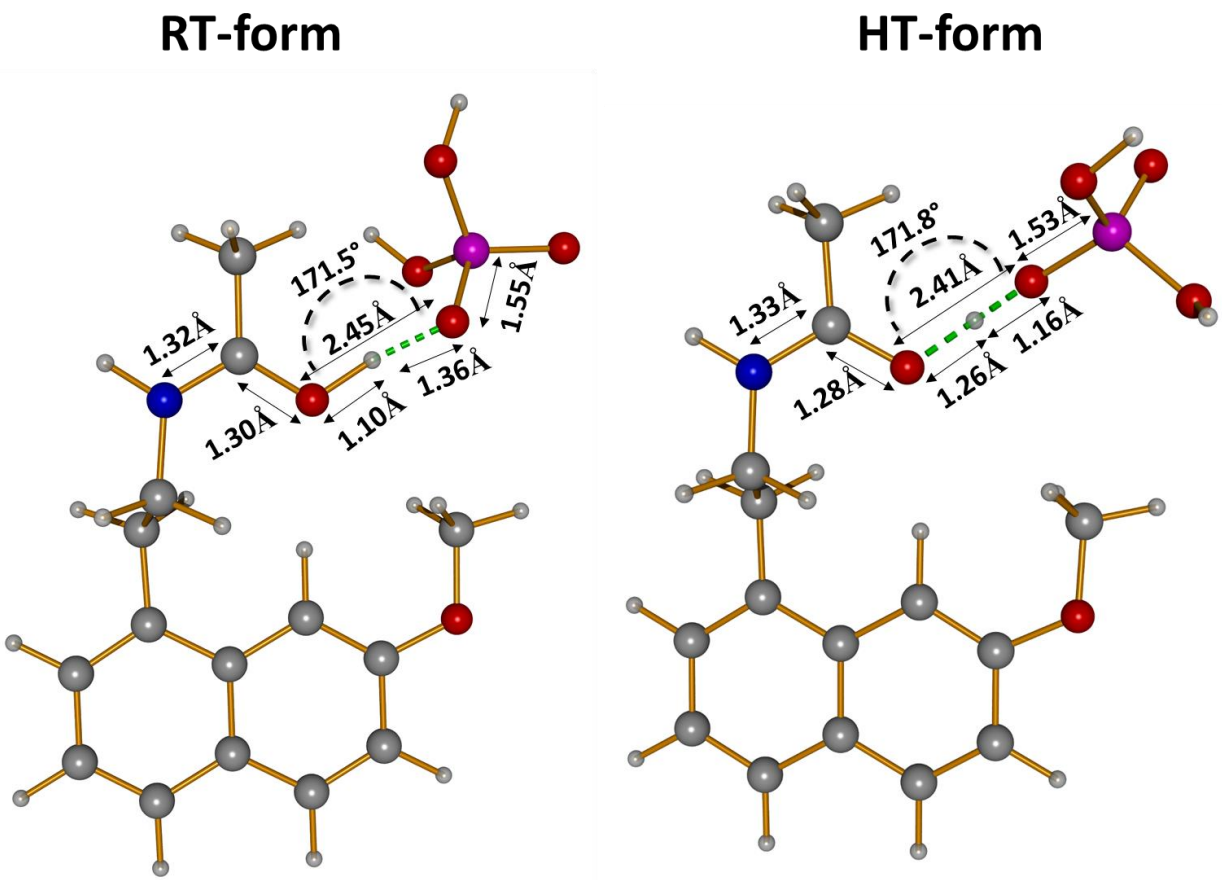

Fig. S6: Representative molecular diagram showing proton shift between Agomelatine and Phosphoric molecules in RT-form and HT-form and the associated bond distances and angle matrix.

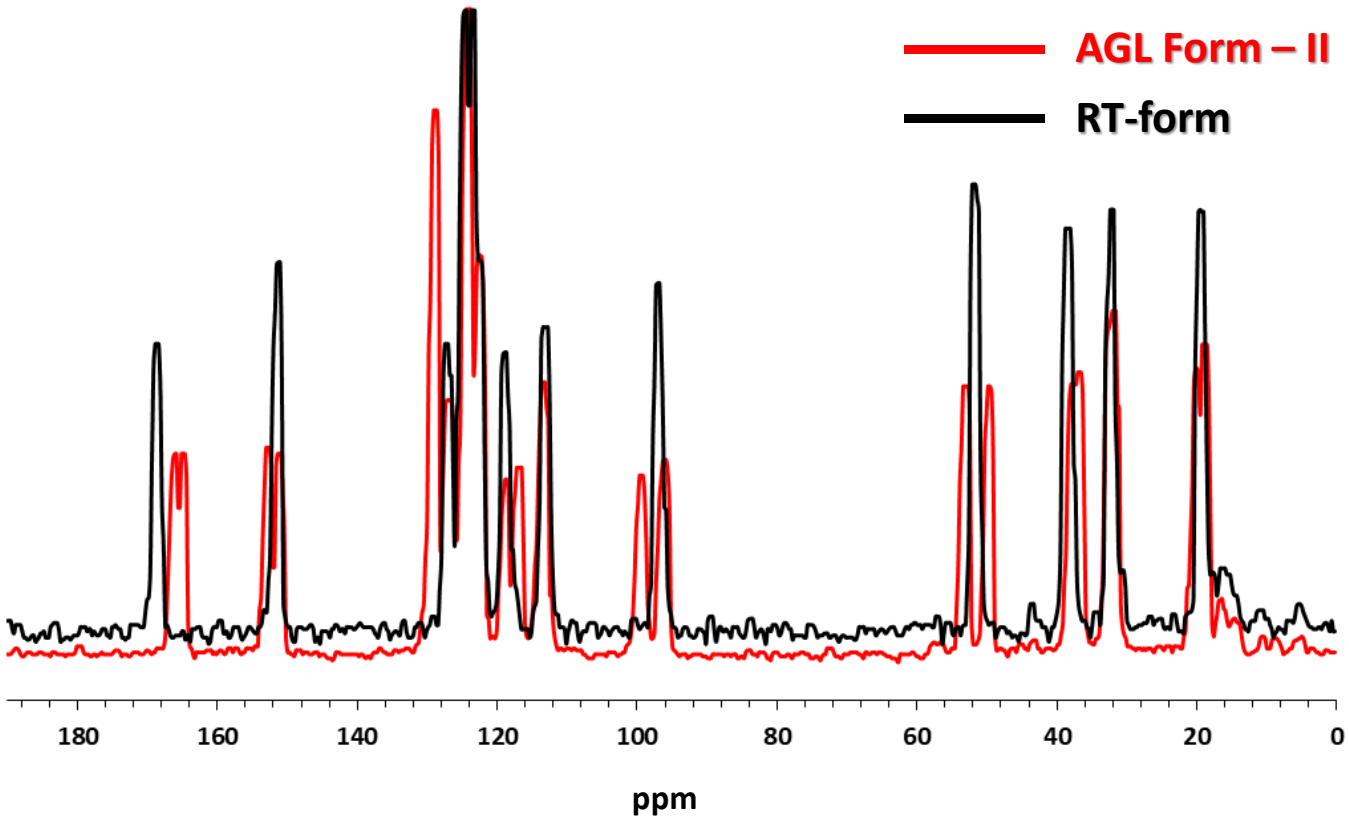

Fig. S7: Overlay of solid-state ^{13}C NMR spectrum of Agomelatine form-II and AGL-P RT-form.

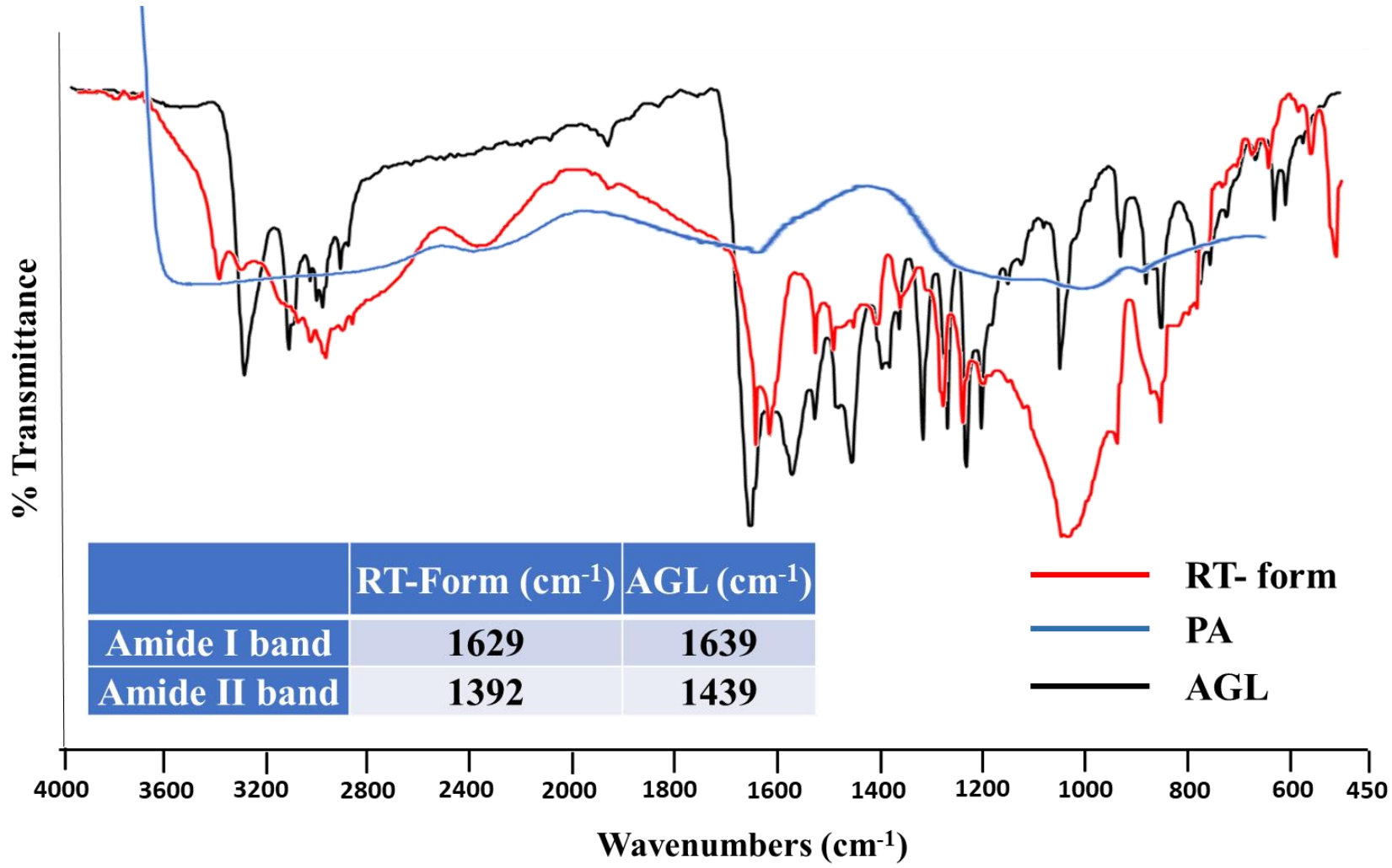

Fig. S8: Overlay of experimental FT-IR spectrum of AGL, Phosphoric acid (PA), and RT-form. Wavenumbers for Amide-I and Amide-II band are listed in the table.

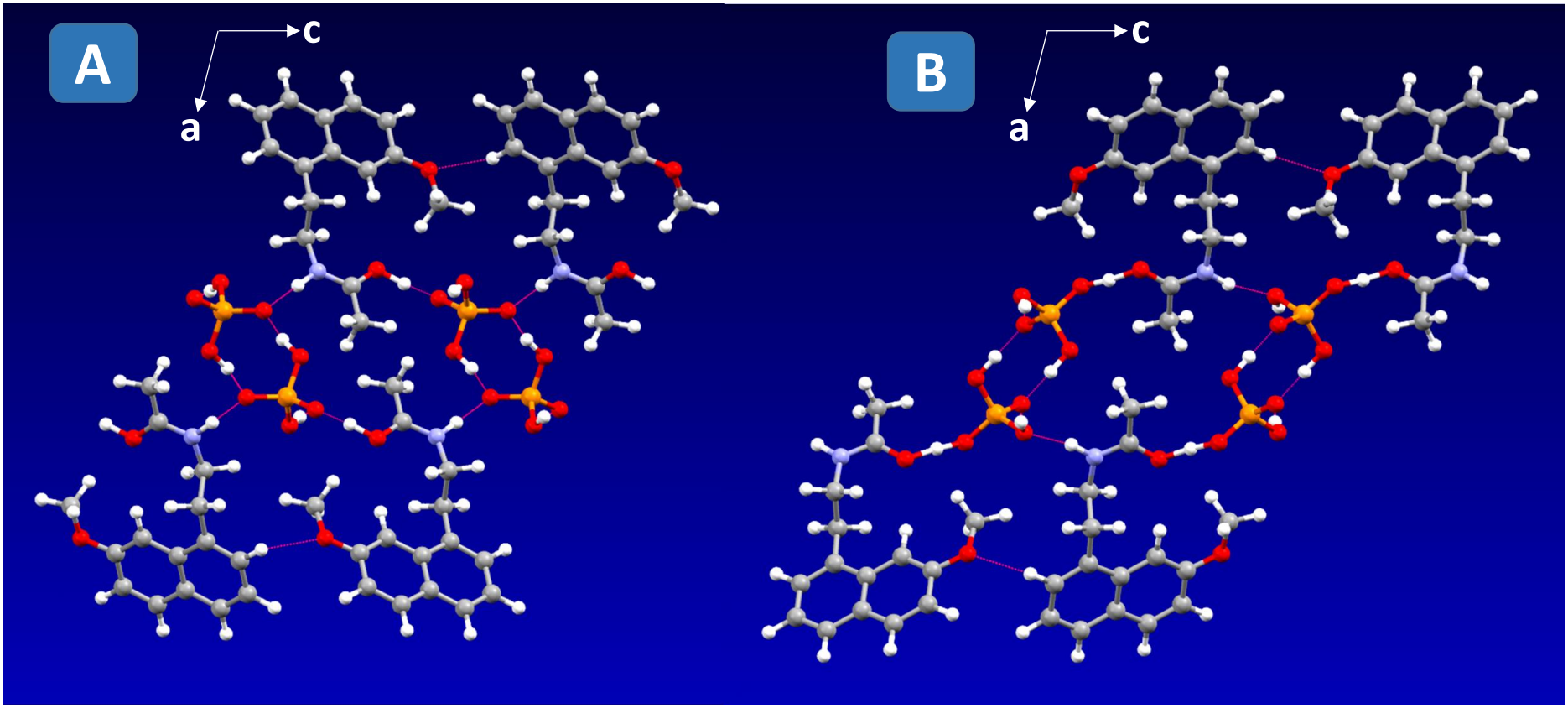

Fig. S9: Crystal packing diagram showing possible hydrogen bonding interactions for RT-form (A) and HT-form (B).

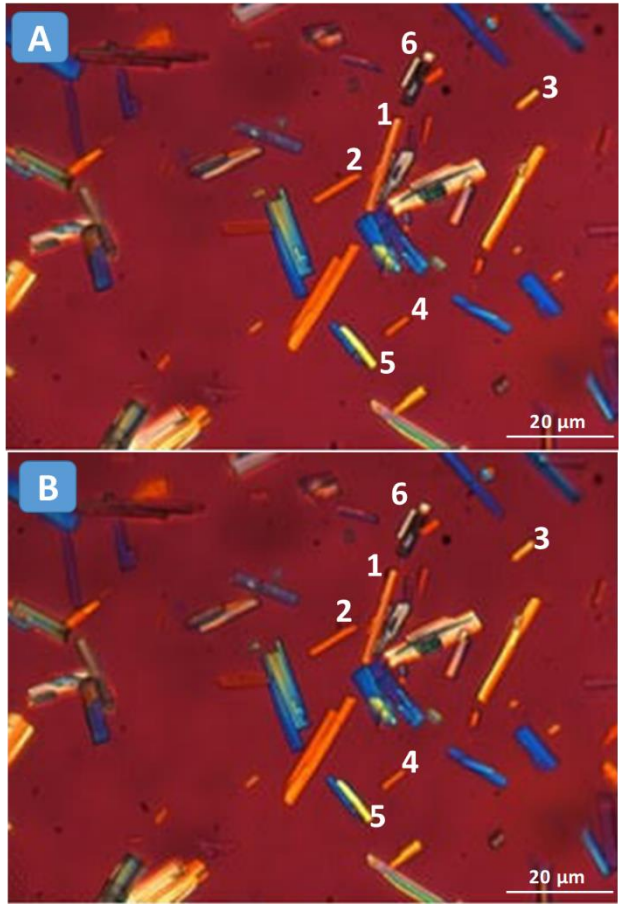

(C) Crystal Size Measurement Table		
Particle No	Particle size (µm)	
	RT-form	HT-form
1	18.9	18.8
2	10.4	10.2
3	5.3	5.1
4	5.2	4.9
5	10.2	10.0
6	6.0	5.6

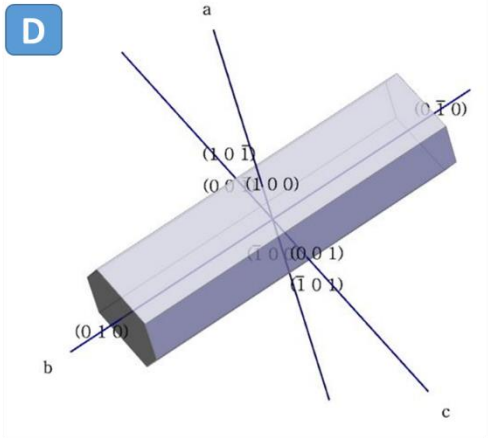

Fig. S10: Image analysis of HSM pictures RT-form (A) and HT-form (B). (C) Table for crystal size measured along with long the major axis. (D) Simulated crystal morphology for RT and HT forms. Upon comparison of predicted morphology with AGL-P crystal shape, the indexed miller facets were unambiguously assigned to the crystal morphology. According to the BFDH calculations, the growth rate and morphological importance for {010} is observed more compared to the {100} and {001} facets. Therefore, the major-axis is equivalent to the b-axis.

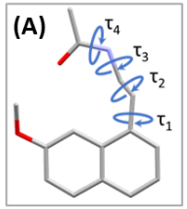

(B) Torsion Angles Table for AGL

AGL Structure	τ_1	τ_2	τ_3	τ_4
RT-form	101.97	171.66	93.73	177.57
HT-form	101.17	176.32	83.88	178.00

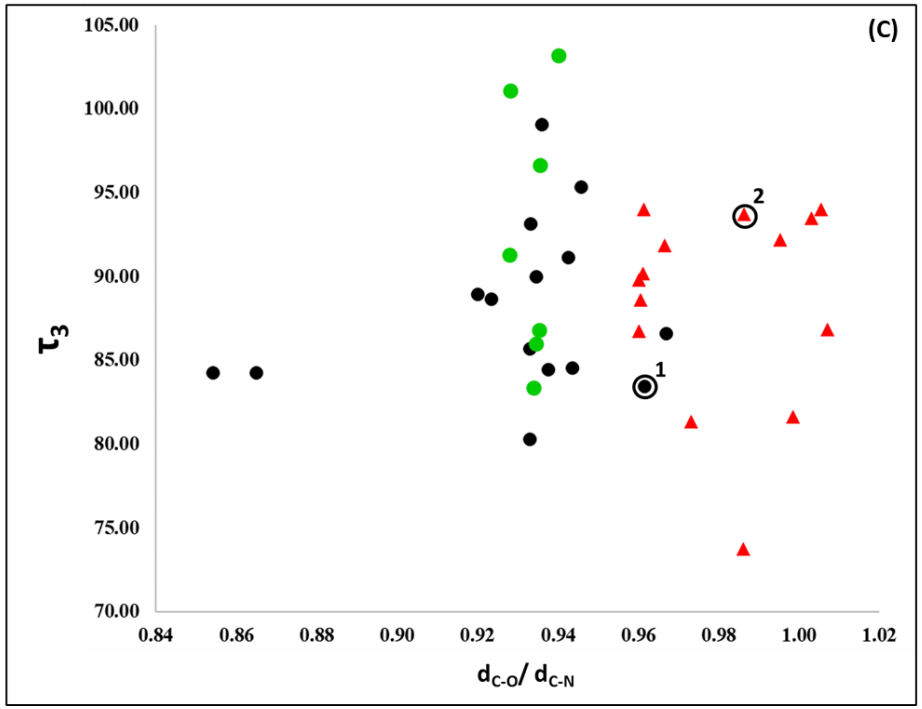

Fig. S11: (A) Molecular structure of Agomelatine showing four possible torsion angles. (B) All torsion angle values for RT and HT-forms are tabulated. (C) A plot between τ_3 and $d_{C\text{-}O}/d_{C\text{-}N}$ from the crystal structures reported with AGL M-APIs as one of its components. Circles (●) indicate co-crystal, red triangles (▲) indicate salt, and green circles (●) indicate pure AGL polymorph. Data points corresponding to 1: HT-form and 2: RT-form are indicated.

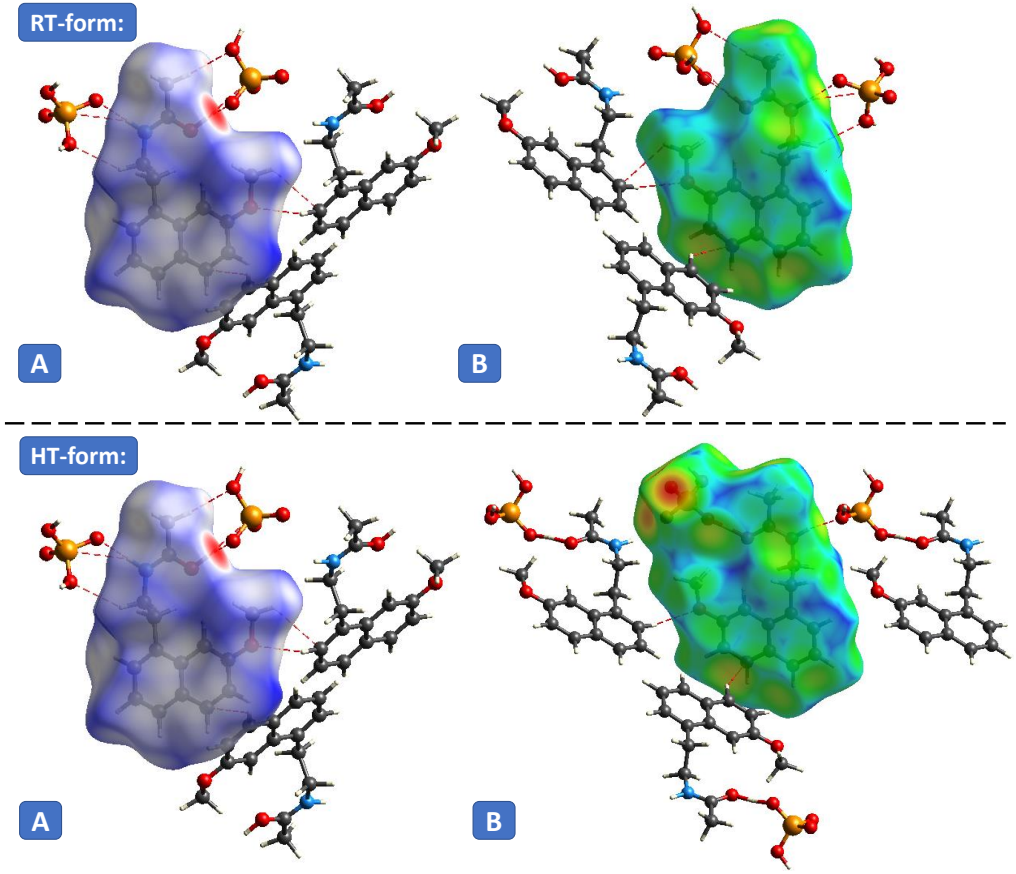

Fig. S12: Comparison of Hirshfeld surface analysis and molecular interactions for RT-form and HT-form. (A) Surface is normalized with respect to internal and external interactions [d_{norm} with colour scale: -0.8 (red) to 1.4 (blue)] (B) Surface with respect to external interactions only [d_e colour scale: 0.5 (red) to 2.5 (blue)].

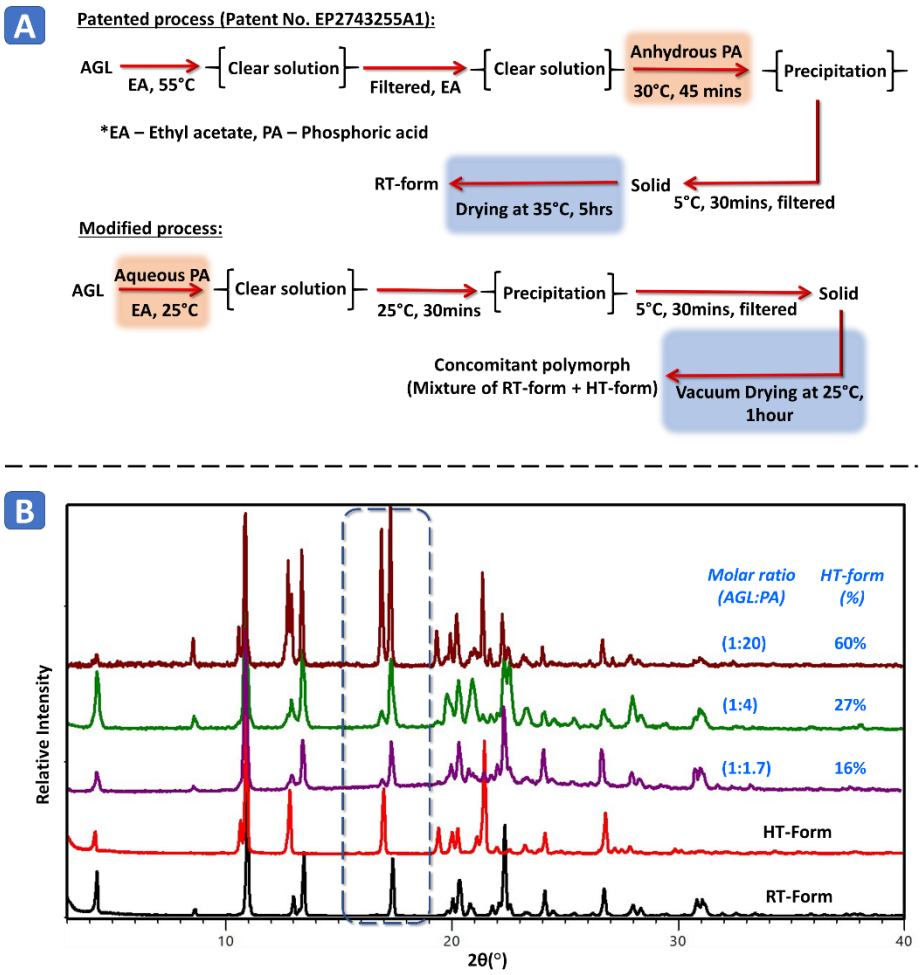

Fig. S13: (A) Comparison of crystallization schematics for optimized patented process and modified current process. Differentiating steps were highlighted, namely H_3PO_4 regent grade (red) and drying step (blue). (B) Overlay of powder-XRD data of three experimental trials showing the concomitant formation of RT and HT-forms. However, a trend of increasing in HT-form content with H_3PO_4 was noticed.